Finsler-Laplace-Beltrami Operators with Application to Shape Analysis

Supplementary Material

This supplementary material is organized as follows:
Sec. 1 provides some proofs concerning properties of Randers metrics mentioned in the main paper: positivity, dual formula, and bounded norm of the dual Randers vector field.
Sec. 2 details the proof of Proposition 1.
Sec. 3 gives additional details about runtime in our experiments.
Sec. 4 shows additional visual results of anisotropic kernels and shape correspondence.

1. Classical proofs for the Randers metric

The proofs in this section of the supplementary material are not novel in the Randers metric community. The purpose of putting them here is to present a self-contained theory that is fully and simply explained, avoiding the need for readers to search through other challenging mathematical papers. For prior existing proofs, see for example [32]. Note that errors exist in various reference materials, which further justifies rederiving the proofs. For instance, in [32] the formulae for the dual Randers metric in Prop. 5.1 are incorrect.

1.1. Proof of Randers metric positivity

Any vector in the tangent space T_xX can be given in the form $M(x)^{-1}v$. We can then write

$$\mathcal{F}_x(M(x)^{-1}v) = \sqrt{v^\top M(x)^{-1}v} + \omega(x)^\top M(x)^{-1}v \tag{41}$$

$$= \|M(x)^{-\frac{1}{2}}v\| + \langle M(x)^{-\frac{1}{2}}\omega(x), M(x)^{-\frac{1}{2}}v\rangle. \tag{42}$$

Using the Cauchy-Schwartz inequality, we get $|\omega(x)^\top M(x)^{-1}v| \leq \|M(x)^{-\frac{1}{2}}\omega(x)\|\|M(x)^{-\frac{1}{2}}v\|$. The assumption on ω provides $\|M(x)^{-\frac{1}{2}}\omega(x)\| < 1$, thus as soon as $v \neq 0$, we get $\mathcal{F}_x(M(x)^{-1}v) > 0$. □

1.2. Proof of dual Randers metric formulae

For conciseness, we drop the explicit dependence on x. The dual Finsler metric $\mathcal{F}^*$ of the Randers metric $\mathcal{F}$ is given by Definition 3. By positive homogeneity of $\mathcal{F}$, it is also given by

$$\mathcal{F}^*(v) = \max\left\{\frac{\langle v, b\rangle}{\mathcal{F}(b)}; b \neq 0\right\}. \tag{43}$$

As such, $\frac{1}{\mathcal{F}^*(v)} = \min\left\{\frac{\mathcal{F}(b)}{\langle v,b\rangle}; b \neq 0\right\}$, and once again by homogeneity we have

$$\frac{1}{\mathcal{F}^*(v)} = \min\{\mathcal{F}(b); \langle v, b\rangle = 1\}. \tag{44}$$

The Lagrangian for this constrained optimization problem is given by $L(b, \mu) = \mathcal{F}(b) + \mu\langle v, b\rangle$. Computing the gradient $\frac{\partial L}{\partial b}$ and setting it to 0 to satisfy the KKT conditions, the optimal b, denoted b^*, satisfies

$$M\frac{b^*}{\|b^*\|_M} + \omega + \mu v = 0. \tag{45}$$

On one hand, by computing the scalar product with b^*, and recalling that the constraint enforces $\langle v, b^*\rangle = 1$, and recalling the formula for the Randers metric (Eq. (19)) we get $\mu = -\mathcal{F}(b^*)$. Since b^* solves the optimization problem in Eq. (44), we have

$$\mu = -\frac{1}{\mathcal{F}^*(v)}. \tag{46}$$

On the other hand, we can compute $\|\omega + \mu v\|_{M^{-1}}$ from Eq. (45)

$$\|\omega + \mu v\|_{M^{-1}} = \frac{\|Mb^*\|_{M^{-1}}}{\|b^*\|_M} = 1. \tag{47}$$

Taking the square, we get a degree two polynomial for which μ is a root

$$\mu^2\|v\|^2_{M^{-1}} + 2\mu\langle\omega, v\rangle_{M^{-1}} + \|\omega\|^2_{M^{-1}} - 1 = 0. \tag{48}$$

Writing $\alpha = 1 - \|\omega\|^2_{M^{-1}} > 0$, the roots are given by

$$\mu_\pm = \frac{-\langle\omega, v\rangle_{M^{-1}} \pm \sqrt{\langle\omega, v\rangle^2_{M^{-1}} + \|v\|^2_{M^{-1}}\alpha}}{\|v\|^2_{M^{-1}}}. \tag{49}$$

Clearly, $\mu_+ > 0$ and $\mu_- < 0$ for $v \neq 0$, yet $\mu < 0$ following $\mu = -\mathcal{F}(b^*)$ as the metric is always positive. Therefore $\mu = \mu_-$, and then by inverting Eq. (46) we get

$$\mathcal{F}^*(v) = \frac{\|v\|^2_{M^{-1}}}{\langle\omega, v\rangle_{M^{-1}} + \sqrt{\langle\omega, v\rangle^2_{M^{-1}} + \|v\|^2_{M^{-1}}\alpha}} \tag{50}$$

$$= \sqrt{v^\top \frac{1}{\alpha^2}\left(\alpha M^{-1} + M^{-1}\omega\omega^\top M^{-1}\right)v} - \frac{1}{\alpha}\langle\omega, v\rangle_{M^{-1}}, \tag{51}$$

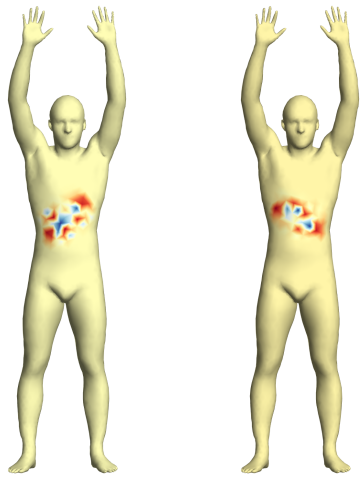

Figure 5. Finsler-based anisotropic kernels $g_{\alpha\theta,x}$ centered at the same point x with different rotation angles θ equal to 0 (left) and $\frac{3\pi}{8}$ (right). Here the filter is chosen to be the Chebychev polynomial $\hat{g}(\lambda) = T_5(\lambda)$.

where we used the classical trick $\frac{1}{x+\sqrt{y}} = \frac{x-\sqrt{y}}{x^2-y}$ to remove the square root from the denominator. We now recognise the dual metric $\mathcal{F}^*$ of the Randers metric $\mathcal{F}$ as a Randers metric associated to (M^*, ω^*) with

$$\begin{cases} M^* = \frac{1}{\alpha^2}(\alpha M^{-1} + (M^{-1}\omega)(M^{-1}\omega)^\top), \\ \omega^* = -\frac{1}{\alpha}M^{-1}\omega. \end{cases} \quad \square \quad (52)$$

1.3. Proof of $\|\omega^*\|_{M^{*-1}(x)} < 1$

For conciseness, we drop the explicit dependence on x and we denote $\tilde{\omega} = M^{-\frac{1}{2}}\omega$. Recalling that M is symmetric and that $\alpha > 0$, and plugging $M^{-1}\omega = M^{-\frac{1}{2}}\tilde{\omega}$ into Eqs. (22) and (23), we get

$$\|\omega^*\|^2_{M^{*-1}} = \tilde{\omega}^\top(\alpha I + \tilde{\omega}\tilde{\omega}^\top)^{-1}\tilde{\omega}. \quad (53)$$

We then invoke the Sherman-Morrison formula $\left(A + uv^\top\right)^{-1} = A^{-1} - \frac{1}{1+v^\top A^{-1}u}A^{-1}uv^\top A^{-1}$ for matrix $A = I$ and vectors $u = v = \alpha^{-\frac{1}{2}}\tilde{\omega}$. Writing $q_{M,\omega} = \alpha^{-1}\tilde{\omega}^\top\tilde{\omega} = \alpha^{-1}\omega^\top M^{-1}\omega$ for conciseness, we get

$$\|\omega^*\|^2_{M^*(x)^{-1}} = q_{M,\omega}\left(1 - \frac{q_{M,\omega}}{1+q_{M,\omega}}\right) \quad (54)$$

$$= \frac{q_{M,\omega}}{1+q_{M,\omega}} \quad (55)$$

$$= 1 - \frac{1}{1+\alpha^{-1}\omega^\top M^{-1}\omega} < 1. \quad \square \quad (56)$$

2. Proof of Proposition 1

For conciseness, we drop the explicit dependence on x. Denoting $\mathcal{P}(u) = \mathcal{F}^*(\nabla u)\nabla\mathcal{F}^*(\nabla u)$, the Finsler heat equation is given by

$$\partial_t u = \operatorname{div}(\mathcal{P}(u)). \quad (57)$$

Differentiating the Finsler dual metric Eq. (24), we have

$$\nabla\mathcal{F}^*(\nabla u) = M^*\frac{\nabla u}{\|\nabla u\|_{M^*}} + \omega^*. \quad (58)$$

Given the initial condition, the solution u will approximately satisfy $\mathcal{F}^*(\nabla u) = 1$ in short time, i.e. for small time steps t. As such, in short time we have

$$\mathcal{P}(u) = M^*\frac{\nabla u}{\|\nabla u\|_{M^*}} + \omega^*. \quad (59)$$

Following [5] (Corrolary 2.10), if u follows this condition, then there exists a positive scalar λ giving the proportionality between the following vectors

$$M^*\frac{\nabla u}{\|\nabla u\|_{M^*}} + \omega^* = \lambda\big((M^* - \omega^*\omega^{*\top})\nabla u + \omega^*\big). \quad (60)$$

This is due to the fact that ∇u belongs to the shared 0-level set of functions of v on the tangent space $f_1(v) = \|v\|_{M^*} + \omega^{*\top}v - 1$ and $f_2(v) = \|v\|^2_{M^* - \omega^*\omega^{*\top}} + 2\omega^{*\top}v - 1$ which share the same sign for all v, and with gradients computed at $v = \nabla u$ equal to $\nabla f_1(\nabla u) = M^*\frac{\nabla u}{\|\nabla u\|_{M^*}} + \omega^*$ and $\nabla f_2(\nabla u) = 2((M^* - \omega^*\omega^{*\top})\nabla u + \omega^*)$. By computing the scalar product of Eq. (60), i.e. of the equation $\nabla f_1(\nabla u) = \frac{\lambda}{2}\nabla f_2(\nabla u)$, with ∇u, and recalling that $\mathcal{F}^*(\nabla u) = 1$, we have that

$$\nabla u^\top\nabla f_1(\nabla u) = \mathcal{F}^*(\nabla u) = 1 \quad (61)$$

and that

$$\nabla u^\top\frac{1}{2}\nabla f_2(\nabla u) = \|\nabla u\|^2_{M^* - \omega^*\omega^{*\top}} + (1 - \|\nabla u\|_{M^*}) \quad (62)$$

$$= \|\nabla u\|^2_{M^*} - (1 - \|\nabla u\|_{M^*})^2 + (1 - \|\nabla u\|_{M^*}) \quad (63)$$

$$= \|\nabla u\|_{M^*}. \quad (64)$$

Another calculation gives us that

$$1 + \|\nabla u\|^2_{M^* - \omega^*\omega^{*\top}} = 1 + \|\nabla u\|^2_{M^*} - (1 - \|\nabla u\|_{M^*})^2 \quad (65)$$

$$= 2\|\nabla u\|_{M^*}, \quad (66)$$

thus $\nabla u^\top\frac{1}{2}\nabla f_2(\nabla u) = \frac{1}{2}(1 + \|\nabla u\|^2_{M^* - \omega^*\omega^{*\top}})$. As $\nabla f_1(\nabla u) = \frac{\lambda}{2}\nabla f_2(\nabla u)$, we can deduce that

$$\lambda = \frac{2}{1 + \nabla u^\top(M^* - \omega^*\omega^{*\top})\nabla u}. \quad (67)$$

Under the assumption that the metric is close to Riemannian, i.e. $\|\omega\|$ is small, then we can approximate $\|\nabla u\|_{M^*} = \mathcal{F}^*(\nabla u) = 1$, and thus approximate the proportionality coefficient λ by

$$\lambda = \frac{2}{1 + \|\nabla u\|_{M^*}} = 1. \tag{68}$$

Using Eqs. (59) and (60), we conclude that for this particular initialisation the heat equation becomes in short time

$$\partial_t u = \operatorname{div}\left((M^* - \omega^* {\omega^*}^\top)\nabla u\right) + \operatorname{div}(\omega^*). \quad \square \tag{69}$$

3. Implementation and runtime

In terms of runtime and memory, the difference with [29] comes from a small overhead due to computing the metric as preprocessing. Our additional actions involve cheap basic operations on 3×3 matrices, e.g. inversion (Eq. (37)) and multiplication (Eqs. (22), (23), (36) and (38)). Note that further preprocessing operations, e.g. Eq. (39), are the same as those in [29] and thus have the same cost. For example, our implementation on a CPU '2 GHz Intel Core i5' takes on average 1.70s per shape in the FAUST (Remeshed) dataset (1.82s per shape in the SCAPE (Remeshed) dataset), compared to 1.55s (resp. 1.76s) for [29]. Once this preprocessing is performed, we obtain an anisotropic LBO discretised as a matrix (line 432) of the same size as in [29]. Therefore, runtime of the core shape-matching learning algorithm is the same and is significantly longer, around 30s per epoch for FAUST (Remeshed) (resp. 10s for SCAPE (Remeshed)) on 1 GPU 'Quadro P6000'.

4. Further visual results

4.1. Example kernels

We show in Fig. 5 two of our anisotropic kernels $g_{\alpha\theta,x}$ at different angles, when choosing a predetermined Chebychev polynomial for its spectral decomposition.

4.2. More shape correspondence results

We display further visual shape correspondence results in Figs. 6 to 9. Our method clearly outperforms FieldConv while providing on par visual results to ACSCNN. The superiority of our method is revealed in the quantitative results of the main paper.

Figure 6. Visual shape correspondence results on the FAUST Remeshed dataset. The source shape is on the left, on which we perform dense correspondence estimation on the shapes to the right, using either FieldConv, ACSCNN, or our approach.

Figure 7. Visual shape correspondence results on the SCAPE Remeshed dataset. The source shape is on the left, on which we perform dense correspondence estimation on the shapes to the right, using either FieldConv, ACSCNN, or our approach.

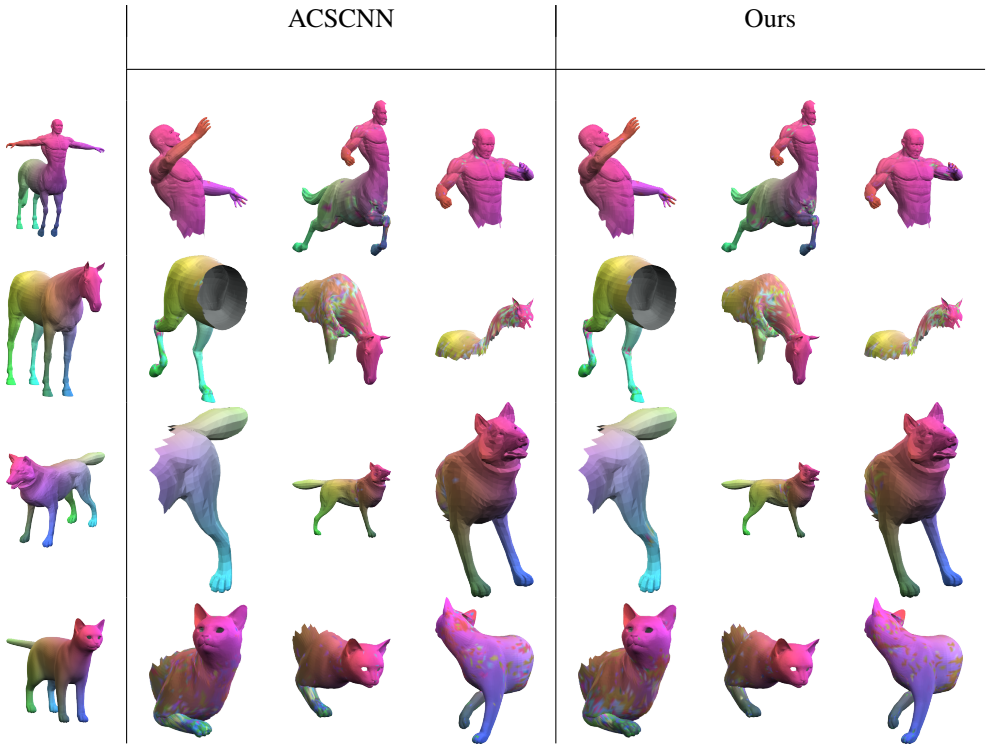

Figure 8. Visual shape correspondence results on the SHREC'16 Cuts dataset. The source shape is on the left, on which we perform dense correspondence estimation on the shapes to the right, using either ACSCNN or our approach. FieldConv fails to provide meaningful correspondence results on partial shapes so we do not display its qualitative performance.

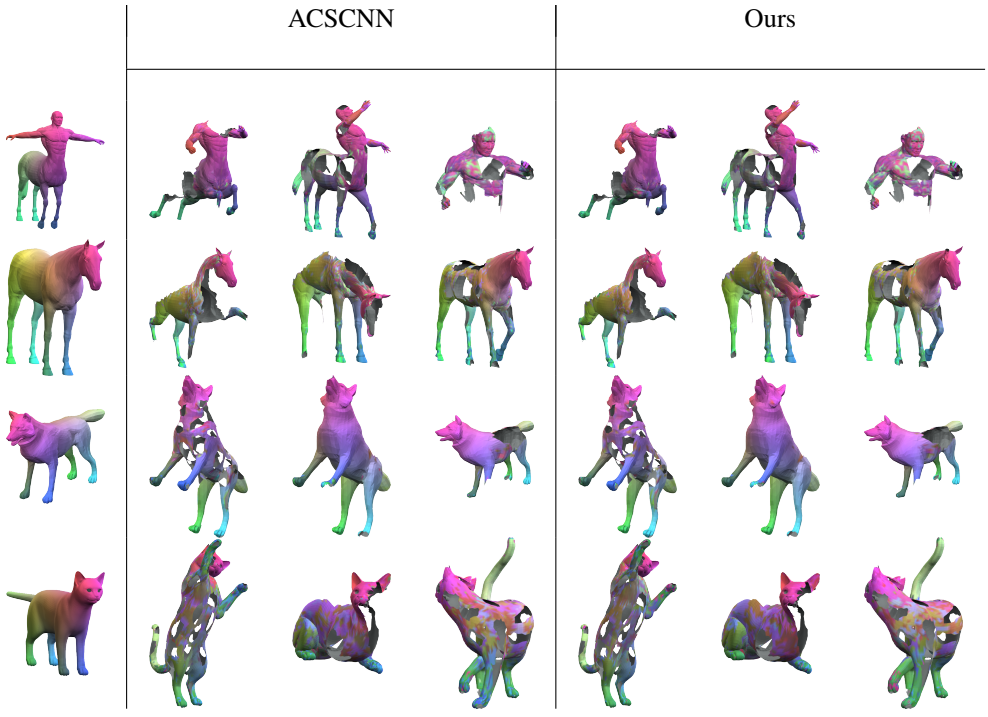

Figure 9. Visual shape correspondence results on the SHREC'16 Holes dataset. The source shape is on the left, on which we perform dense correspondence estimation on the shapes to the right, using either ACSCNN or our approach. FieldConv fails to provide meaningful correspondence results on partial shapes so we do not display its qualitative performance.